Journal of
Synchrotron
Radiation

ISSN 0909-0495

Received 4 October 2010
Accepted 11 March 2011

BioCARS: a synchrotron resource for time-resolved X-ray science

T. Graber,[a]* S. Anderson,[a]‡ H. Brewer,[a] Y.-S. Chen,[a] H. S. Cho,[b] N. Dashdorj,[b] R. W. Henning,[a] I. Kosheleva,[a] G. Macha,[a] M. Meron,[a] R. Pahl,[a] Z. Ren,[a] S. Ruan,[a] F. Schotte,[b] V. Šrajer,[a] P. J. Viccaro,[a] F. Westferro,[a] P. Anfinrud[b] and K. Moffat[a]

[a]Center for Advanced Radiation Sources, The University of Chicago, Chicago, IL 60637, USA, and [b]NIDDK, National Institutes of Health, Bethesda, MD 20892, USA.
E-mail: graber@cars.uchicago.edu

BioCARS, a NIH-supported national user facility for macromolecular time-resolved X-ray crystallography at the Advanced Photon Source (APS), has recently completed commissioning of an upgraded undulator-based beamline optimized for single-shot laser-pump X-ray-probe measurements with time resolution as short as 100 ps. The source consists of two in-line undulators with periods of 23 and 27 mm that together provide high-flux pink-beam capability at 12 keV as well as first-harmonic coverage from 6.8 to 19 keV. A high-heat-load chopper reduces the average power load on downstream components, thereby preserving the surface figure of a Kirkpatrick–Baez mirror system capable of focusing the X-ray beam to a spot size of 90 μm horizontal by 20 μm vertical. A high-speed chopper isolates single X-ray pulses at 1 kHz in both hybrid and 24-bunch modes of the APS storage ring. In hybrid mode each isolated X-ray pulse delivers up to $\sim 4 \times 10^{10}$ photons to the sample, thereby achieving a time-averaged flux approaching that of fourth-generation X-FEL sources. A new high-power picosecond laser system delivers pulses tunable over the wavelength range 450–2000 nm. These pulses are synchronized to the storage-ring RF clock with long-term stability better than 10 ps RMS. Monochromatic experimental capability with Biosafety Level 3 certification has been retained.

Keywords: synchrotron beamline; Laue crystallography; time-resolved crystallography; X-ray optics.

1. Introduction

BioCARS, a national user facility for time-resolved Laue and monochromatic macromolecular crystallography, is located at sector 14 of the Advanced Photon Source (APS) at Argonne National Laboratory, and is supported by the National Center for Research Resources, NIH. This facility consists of a bending-magnet (BM) and an insertion-device (ID) beamline with one experimental station for each beamline. The ID beamline has recently undergone an extensive upgrade that included a new X-ray source, a complete redesign of the X-ray optics, construction of a second optics enclosure (SOE), upgraded instrumentation for the time-resolved (TR) research program, and the addition of a regenerative-amplifier/optical-parametric amplifier (RA/OPA) laser system that enables 100 ps time-resolved measurements for the first time at this facility.

One of the scientific areas of emphasis at BioCARS has been time-resolved macromolecular crystallography, particularly using Laue techniques. This field was pioneered at MacCHESS (Moffat *et al.*, 1984; Moffat, 1989), developed at NSLS (Genick *et al.*, 1997), extended to the nanosecond time range at ID09 (ESRF) and at BioCARS (APS) (Bourgeois *et al.*, 1996, 2003; Šrajer *et al.*, 1996, 2001; Perman *et al.*, 1998; Ren *et al.*, 1999, 2001; Anderson *et al.*, 2004; Rajagopal *et al.*, 2004; Ihee *et al.*, 2005; Schmidt *et al.*, 2005; Knapp *et al.*, 2006) and to the sub-nanosecond time range at ID09 (ESRF) (Wulff *et al.*, 2002; Schotte *et al.*, 2003, 2004; Bourgeois *et al.*, 2006). More recently the NW14A beamline at the Photon Factory Advanced Ring achieved 100 ps resolution as well (Nozawa *et al.*, 2007). The first nanosecond time-resolved macromolecular crystallography experiments on the BioCARS ID beamline were conducted in 2000. The recent ID upgrade was designed to enhance the capabilities for time-resolved pump–probe measurements by fully utilizing the extraordinary beam properties provided by the APS, a third-generation synchrotron source. The goals for the upgrade were fourfold: to produce the highest-quality Laue diffraction data possible during standard readily available operating modes of the APS; to enable experiments in which as few X-ray pulses as possible,

‡ Current Address: Life Sciences Collaborative Access Team, 9700 South Cass Avenue, Bldg 436A, Argonne, IL 60439, USA.

perhaps only a single pulse, are required; to extend the time resolution of experiments conducted at the beamline from a few nanoseconds to ∼100 ps; and to maintain capabilities for excellent monochromatic data collection, particularly on crystals of biohazards at the BSL2 and BSL3 level.

A prototypical TR measurement based on the pump–probe technique is illustrated in Fig. 1. Reaction initiation by laser pulse excitation (pump) is followed after a suitable time delay by an X-ray pulse (probe) that measures the state of the system at that instant. Individual pulses from the synchrotron are isolated by an X-ray beam chopper system synchronized to the storage-ring RF clock. A laser pulse propagating orthogonally to the X-ray pulse intersects the X-ray beam at the sample which is positioned at the center of a goniometer. The time dependence of the system is examined by varying the time delay between the pump and probe pulses over the entire course of the reaction. Key to this method is the ability to isolate a single X-ray pulse from the synchrotron pulse train. Fig. 2 illustrates how this isolation is achieved *via* a series of choppers and a shutter. The isolated X-ray pulses are ∼100 ps in duration in the standard 24-bunch mode of APS operation, which establishes the minimum time resolution attainable with this method. The state of the system is recorded *via* diffraction or scattering of X-rays onto a two-dimensional photon-integrating CCD detector.

We describe here the instrumentation developed to deliver high-flux short-duration X-ray pulses and broadly tunable synchronized picosecond laser pulses to a sample on the 14-ID beamline, and report commissioning studies that demonstrate the new capabilities realised with this major upgrade.

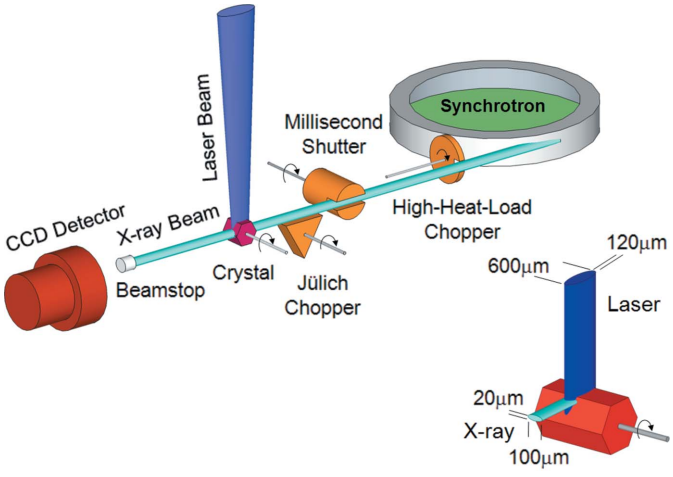

Figure 1
Schematic layout for a typical pump–probe experiment. A mechanical chopper/shutter system is used to isolate single X-ray pulses from the storage ring. The laser beam is oriented orthogonal to the X-ray beam and intersects the crystal at the center of the goniometer rotation. For each crystal orientation, X-ray pulses probe a ∼60–80 μm-deep layer of the crystal on the laser-illuminated side in order to match the typical laser penetration depth. A MAR165 CCD detector records the diffracted X-rays. Typical laser and X-ray beam dimensions are shown in the inset. The vertical size of the X-ray beam can be increased from the 20 μm minimum (shown) to whatever size is necessary to match the laser penetration depth.

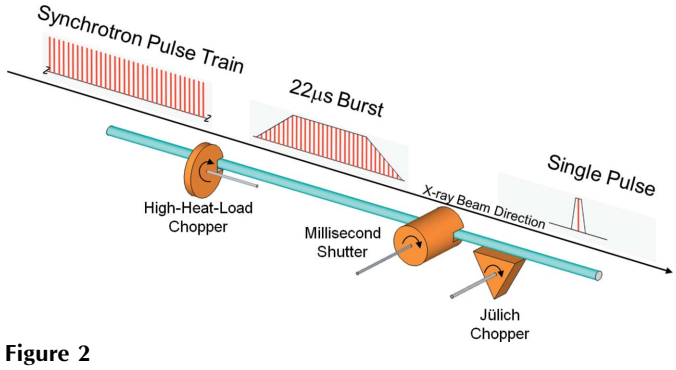

Figure 2
The chopper/shutter system. A high-heat-load chopper reduces power on downstream components to less than 1% of the original power in the X-ray beam. This chopper typically produces a 22 μs burst of X-rays at a repetition rate of 82.3 Hz. The Jülich chopper has a much shorter open time and is capable of isolating a single pulse from the initial synchrotron pulse train at a rate of 1 kHz. Since these choppers are continuously rotating, a shutter with a millisecond open-time acts like the shutter on a photographic camera, exposing the CCD detector on demand to the X-rays scattered by the sample. The millisecond shutter is shown in the open position in the figure. For third-generation synchrotron sources pulse widths are typically ∼100 ps and the inter-bunch spacing is normally 153.4 ns in 24-bunch mode at the APS.

2. Beamline description and characterization

2.1. The X-ray source

For the experiments described in this paper, the probe is a burst of X-rays generated by a single electron bunch or a consecutive series of electron bunches. The RF system in a synchrotron storage ring naturally bunches its highly relativistic electron beam into 'buckets' that circulate with an orbital period determined by the circumference of the ring. This bunching property and the brief temporal width of each bunch make 100 ps time-resolved studies possible. Not all buckets are filled with electrons; it is possible to arrange the electron bunches in a fill pattern where the spacing between bunches is sufficiently large to allow isolation of the radiation from a single bunch by a mechanical chopper. Fig. 3 shows two such fill patterns commonly used at the APS: the hybrid mode and the 24-bunch mode. In the hybrid fill pattern a single electron bunch containing 59 nC (corresponding to a current of 16 mA) is diametrically opposed to eight septuplets that share 317 nC (86 mA). The 1.59 μs gap between the isolated bunch and the nearest bunch in the septuplets facilitates mechanical isolation of the X-ray pulse emitted by the single bunch. Frequent top-up of that single bunch maintains its charge at a level almost fourfold greater than that produced in the 24-bunch standard operating mode at the APS. Improvements to our mirror and shutter system, described in detail in §2.5, allow single pulse isolation for the first time in 24-bunch mode, a feat that is much more demanding owing to the short inter-bunch spacing of 153.4 ns. Since 24-bunch mode and hybrid mode comprise ∼60% and 17%, respectively, of the typical APS run cycle, the total time available for ∼100 ps time-resolved studies has increased fourfold to ∼77% of the run cycle, *i.e.* to more than 3850 h per year.

To maximize the single-pulse X-ray flux, the 14-ID beamline now employs two collinear 2.4 m permanent-magnet (neody-

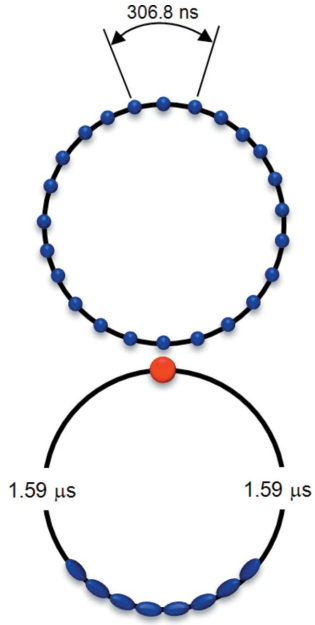

Figure 3
The two APS storage-ring modes used for ∼100 ps time-resolved experiments at BioCARS. The common operating mode has 24 bunches circulating with 4.25 mA per bunch and 153.4 ns separation between the bunches. The bunch length in this mode is 79 ps (FWHM). The hybrid mode has a 16 mA bunch separated from adjacent septuplets by 1.59 µs. The bunch length in this mode is 118 ps (FWHM). There are three 12-week runs per year at the APS, with hybrid mode accounting for ∼17% of the total run cycle and 24-bunch mode accounting for ∼60%. In both modes periodic top-up of the individual bunches maintains the total ring current at 102 mA.

mium iron boron) undulators, U23 and U27, with periods of 23 mm and 27 mm, respectively. The vacuum chamber limits the minimum undulator gap to 10.5 mm. Fig. 4 compares the tuning curve for each of these undulators with that for undulator U33, the source previously used on the beamline and historically the standard insertion device at the APS.

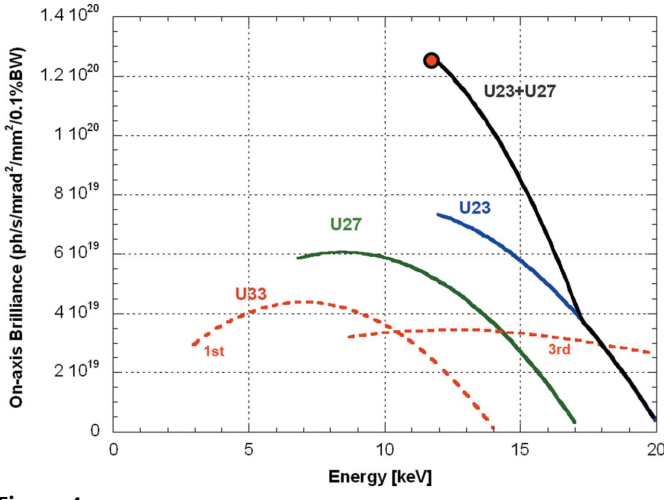

Figure 4
Undulator tuning curves. Both first- and third-harmonic curves are shown for U33 (red dashed lines). This undulator was replaced by a U27 (green solid line) and a U23 (blue solid line). With both undulators tuned to the same energy, their sum (black solid line) peaks at 12 keV (red circle), the normal operating energy for high-flux pink-beam operation.

These short-period undulators were chosen for two reasons: to maximize the total X-ray flux in pink-beam mode when both undulators are tuned to 12 keV; and to provide first-harmonic coverage from 6.8 to 19 keV for monochromatic multi-wavelength anomalous dispersion experiments. We chose 12 keV as our high-flux operating point as a compromise to maximize energy tunability for both pink and monochromatic operation. Though U33 covers a similar energy range, it requires use of the third harmonic to provide energies above ∼13 keV, and therefore suffers from substantial first-harmonic contamination. In contrast, the collinear U23 and U27 combination provides contamination-free first-harmonic coverage over the entire 6.8–19 keV range.

2.2. Layout

The beamline is designed to switch rapidly between three modes of beam delivery: white beam, focused pink beam and focused monochromatic beam. The focused beams offer strong demagnification of 8.3 to 1 horizontally and 5.2 to 1 vertically to yield a minimum beam size of 20 µm vertically by 90 µm horizontally. Fig. 5 presents a schematic view of the beamline; the scale indicates the distance from the source point, *i.e.* the center of the straight section.

A GlidCop power-limiting mask with a 1.5 mm-diameter aperture is located 25.5 m downstream from the source. The size of the aperture and hence the maximum power delivered to the downstream components was constrained by the peak temperature (573 K) allowed by the APS Radiation Safety System for the downstream GlidCop components that have the potential to intercept the beam. To operate within this limit, the collinear U23 and U27 undulators cannot be set to their minimum gaps simultaneously. With both undulators tuned to 12 keV, the maximum power that can be delivered through the aperture to downstream components is ∼520 W. Owing to the energy–angle correlation inherent in undulator radiation, this aperture limits the maximum pink-beam bandwidth to <10% FWHM.

A set of high-heat-load (HHL) slits is located downstream from the mask at 28 m. Since the mirror system images the source at the focus, these slits are analogous to the iris in a photographic camera that cuts out extreme rays and reduces the intensity while preserving the image. Moreover, since the energy–angle correlation in an undulator beam is most pronounced in the vertical direction, the vertical slit can be used to reduce the bandwidth of the undulator harmonic. Indeed, narrowing the vertical aperture to 0.6 mm reduces the transmitted power by approximately a factor of two and narrows the width of the pink beam by almost the same factor. This trade-off is beneficial in pink-beam wide-angle X-ray scattering (WAXS) experiments where the q-space scattering curves are convoluted with the spectral distribution of the undulator.

2.3. X-ray optics

2.3.1. Monochromator. Although the primary mission of the ID beamline is to support dynamics studies utilizing short-

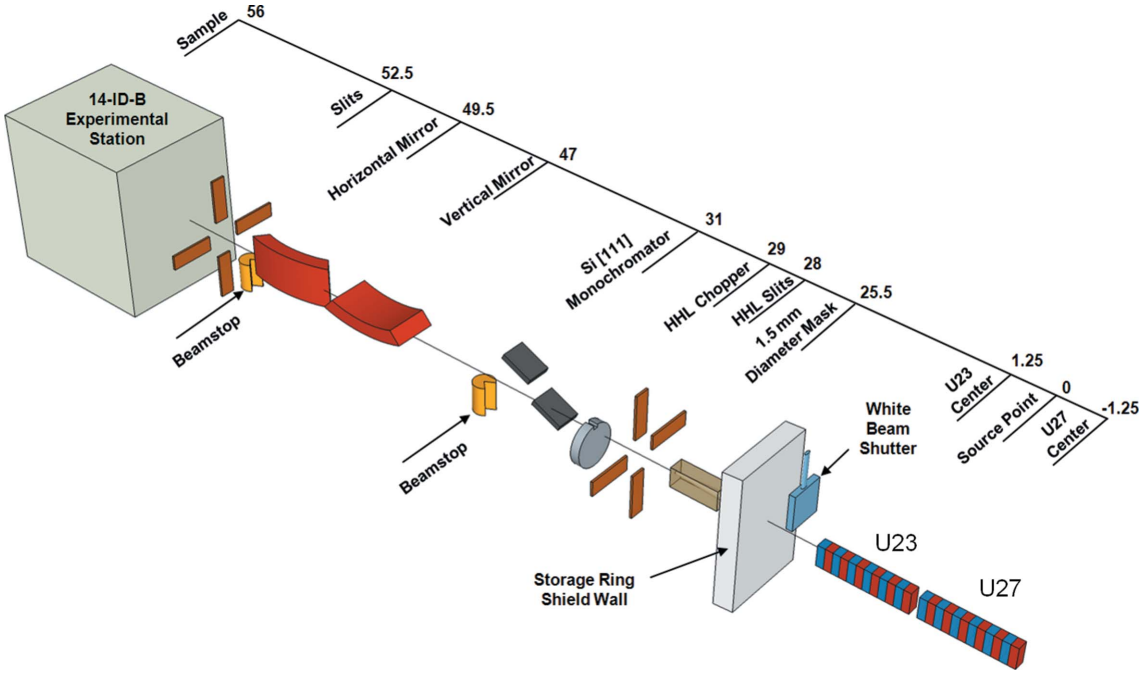

Figure 5
Layout of the upgraded 14-ID beamline. The scale indicates the distance in meters from the source point, *i.e.* between the two insertion devices. From right to left the components are: 1.5 mm-diameter power-limiting mask (25.5 m), high-heat-load slits (28 m), high-heat-load chopper (29 m), Si (111) monochromator (31 m), equipment safety beamstop, vertically focusing mirror (47 m), horizontally focusing mirror (49.5 m), equipment safety beamstop, pink-beam slits (52.5 m) and sample position in the 14-ID-B experimental station (56 m).

pulse pink-beam X-rays, the upgrade retains monochromatic capability, particularly for samples that require our unique Biosafety Level 3 (BSL3) capability. A Kohzu HLD-9BC monochromator with cryogenically cooled silicon (111) crystals can span an energy range of 6.8 to 19 keV (1.82 to 0.65 Å). A fixed-offset beam height of 15 mm is maintained over the entire energy range by slaving the vertical motion of the first crystal with horizontal motion of the second crystal. Both crystals were fabricated, etched and mechanochemically polished by the APS optics group and have identical dimensions of 40 mm (length) × 45 mm (width) × 35 mm (height) with a usable diffraction area of 40 mm × 40 mm. The Kohzu monochromator is located 31 m downstream of the undulators.

An indirectly (contact) cooled crystal mounting geometry is employed for both crystals. This approach was favored over a direct internally cooled geometry owing to its reliability and simplicity. The crystal mounting fixtures are commercially available from Kohzu and are similar to those described by Mochizuki *et al.* (2001). Briefly, each crystal is mounted with 0.5 mm-thick indium foils sandwiched between the sides of the crystal and a water-cooled copper block. After mounting, an X-ray topograph of the entire diffraction surface was measured to assess the degree of strain in the crystal (Krasnicki, 1996). The worst-case residual strain was found to be less than 1.0 arcsec, and the diffraction intensity across the surface of both crystals was found to be uniform throughout the entire rocking curve.

2.3.2. Mirror system. A water-cooled Kirkpatrick–Baez (KB) mirror system was designed to accommodate the direct full-power (520 W) white beam, and to control independently the vertical and horizontal focal planes without changing the mirror angle. Both vertical and horizontal mirror systems were purchased from Oxford-Danfysik (UK); the mirror blanks and benders were subcontracted to SESO (France). Although the nominal operating point of the beamline is 12 keV with 3.8 mrad mirror angles, the mirrors can be tuned from 4 to 2 mrad to achieve a higher X-ray energy cut-off. To accommodate this, the longitudinal length of each mirror is of the order of 1 m in order to accept the X-ray footprint at lower incident angles.

The vertical mirror is upward-deflecting and utilizes a single-actuator U-bender to produce a minimum bend radius of 4 km. The mirror blank was manufactured from single-crystal silicon with overall dimensions of 1030 × 119 × 65 mm. Stripes of rhodium and platinum, 500 Å-thick, were deposited on the blank, producing an optically useful area of 900 × 83 mm. The tangential slope error was measured with a long-trace profiler at SESO and found to be <1 µrad RMS over the usable 900 mm length and <0.9 µrad RMS over 750 mm. The sagittal slope error, measured at five different points along the mirror length, averaged 8.8 µrad RMS. The surface roughness is 2.2 Å RMS.

The vertical mirror was designed to withstand a maximum absorbed power of 500 W without distortion. This heat is extracted through copper fins immersed in gallium–indium eutectic that fills troughs milled into the top surface of the mirror along either side. The copper fins are cooled *via* a temperature-stabilized water-cooling loop.

The mirror bender assembly is positioned using a three-point motorized kinematic mount that combines horizontal and vertical translation with pitch, roll and yaw. The vertical

jacks are positioned with one upstream and the other two downstream. A single piezoelectric actuator is mounted on the upstream side of the mirror above the vertical jack to enable both fine angular adjustment and active stabilization of the vertical position using a PID-controlled feedback loop. The angular resolution of the piezo actuator is 5.5 µrad V^{-1}.

The horizontal mirror deflects the beam inboard towards the storage ring and, like the vertical mirror, utilizes a single-actuator U-bender to produce a somewhat smaller minimum bend radius of 2.5 km, necessary since the horizontal mirror is 2 m closer to the sample. The mirror blank was manufactured from single-crystal silicon with overall dimensions of 1330 × 119 × 50 mm. A single 500 Å-thick rhodium stripe was deposited parallel to a bare silicon stripe, producing an optically useful area of 1000 × 100 mm. The tangential slope error was <1.04 µrad RMS over 900 mm length and <0.9 µrad RMS over the central 750 mm. The sagittal slope error, measured at five different points along the mirror length, averaged 2.44 µrad RMS. The surface roughness is 2.4 Å RMS.

Since the vector normal to the reflecting surface is horizontal (*x*-direction), the cooling geometry had to be modified from the more standard configuration of the vertical mirror. The top of the mirror blank has a slot and fin-cooling geometry similar to the vertical mirror, but the bottom surface has an additional rectangular protrusion that fits into a trough filled with liquid gallium–indium eutectic. In standard operations the bulk of the power is absorbed by the HHL chopper (see §2.5.1), which greatly reduces the power incident on the mirrors to ∼1 W. Cooling the mirrors thus represents a conservative approach that ensures the safety of the mirror system even if the HHL chopper and/or the Equipment Protection System (EPS) were to fail.

2.4. Beamline performance

We critically assessed the beamline performance by comparing measured results with theory. The beamline was designed to permit a direct line-of-sight from the source point at the center of the straight section in the storage ring to the 14-ID-B station. Each optical element can be inserted into or removed from the beam path, thus allowing measurement of the performance of individual elements. Moreover, all ID enclosures are white-beam compatible: their walls were designed with the lead thickness appropriate to shield against high-energy bremsstrahlung radiation, as required by the APS. Thus, the total white-beam power delivered by the undulators to the 14-ID-B station can be measured.

2.4.1. Power measurements. Power measurements were compared with theory for each element in the beamline. Table 1 lists the powers measured for white- and pink-beam operation with several mirror and undulator combinations. *XUS*, the undulator code included in *XOP*, was used to calculate the energy spectrum through the 1.5 mm power-limiting aperture with both U23 and U27 tuned to 12 keV (Sánchez del Río & Dejus, 2004). The total power P is given by the integral of the product of the energy spectrum $S(E)$, the total mirror reflectivity $R(E)$ for both mirrors, and the total absorption $A(E)$ owing to beryllium windows and air paths. Equation (1) represents this integral where $C = 1.6 \times 10^{-19}$ J eV^{-1},

$$P = C \int_0^\infty R(E)A(E)S(E)\,dE. \quad (1)$$

Fig. 6 shows the product $R(E)A(E)$ on the right-hand axis, which can be thought of as a transmission function for the beamline. Both mirrors are set at 3.8 mrad, and 2 mm of beryllium is assumed (to account for four vacuum-isolating windows along the beam path). The curve shows little transmission below 5 keV owing to beryllium absorption and reaches a maximum of 70% at 12 keV, the peak of the undulator first harmonic. The decrease on the high-energy side at 17.5 keV is due to the high-energy cut-off of both mirrors operating at 3.8 mrad incidence angle on the rhodium stripe.

The second row in Table 1 shows the white-beam power for undulators U23 and U27, measured in the 14-ID-B station

Table 1
Beamline power measurements.

Both mirrors are set to 3.8 mrad and the power-limiting aperture is a 1.5 mm-diameter mask.

	U27	U27 Calc	U23	U23 Calc	U27 + U23	U27 + U23 Calc
White beam (W)	142	144	329	319	477	463
V mirror (W)	58	66	90	101	161	167
H mirror (W)	61	66	94	101	152.5	167
V and H mirrors (W)	54.6	58	81.9	89	135	147
24-Bunch (photons $pulse^{-1}$)	–	–	–	–	1.1×10^{10}	1.2×10^{10}
Hybrid (photons $pulse^{-1}$)	–	–	–	–	4.2×10^{10}	4.6×10^{10}

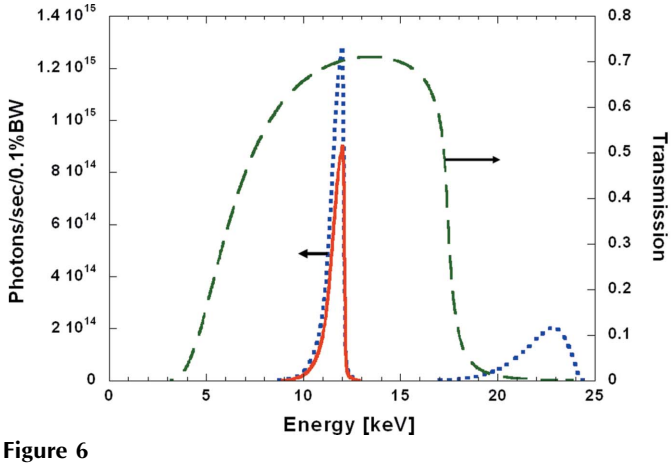

Figure 6
Calculated energy spectrum for the first harmonic of the combined U23 and U27 undulators. The blue dotted curve shows the raw spectrum without any attenuation. The green dashed curve is a beamline transmission function that accounts for mirror reflectivity of rhodium at 3.8 mrad and absorption in beryllium windows. The red solid curve is the product of the green and blue curves and shows the limited attenuation of the first harmonic and near-complete suppression of the second harmonic.

using a thermally isolated copper-block calorimeter with 2 kg mass. A 4.75 mm-diameter 30 mm-deep entrance hole was drilled into the copper block to accept the beam and minimize power lost owing to backscatter. For these measurements the 1.5 mm-diameter mask (Fig. 5, 25.5 m) was the only limiting aperture. Column 2 shows measurement of U27 power alone at 12 keV (K_{27} = 0.92) and column 4 shows the same measurement for U23 alone (K_{23} = 1.16). Column 6 represents the case where both undulators are tuned to 12 keV. The white-beam power measurements in row 2 are within values predicted by theory by a few percent. Power measurements after each mirror individually are given in rows 3 and 4; row 5 gives the result when both mirrors are inserted into the beam. The measured reflectivity of the horizontal mirror is better than that of the vertical mirror by ∼5%. Note that the vertical focusing mirror absorbs most of the power from the high-energy portion of the white beam and produces a pink beam spectrum that is almost totally reflected by the horizontal focusing mirror. This accounts for the relatively small reduction in power when going from the single-mirror to the double-mirror case.

The total number of photons per pulse can be found by dividing the energy spectrum $S(E)$ in equation (1) by $\hbar\omega$ and integrating. Rows 6 and 7 give the number of photons per pulse for both 24-bunch and hybrid modes. The quantitative power measurements given in Table 1 establish that each beamline component and the beamline as a whole is performing as specified, and provide baseline data against which measurements during routine operations can be compared.

2.4.2. Focal spot size. The focal spot formed by the KB mirror system represents a demagnified image of the radiative source after broadening by non-idealities in the mirror system. The most important contributions to the focal spot size are the first-order coma, the third-order spherical aberration and the fabrication slope error (Susini & Wulff, 1993 1993; Susini, 1995; Uruga *et al.*, 2001). These contributions to the focal spot size can be estimated by equation (2),

$$\begin{aligned} F_{\rm Coma} &= 2.35\Sigma M, \\ F_{\rm Spherical} &= \frac{3}{16}L^2\frac{\theta_i}{p}\frac{(1-M^2)}{M}, \\ F_{\rm Fabrication} &= 2(2.35\Delta_{\rm Fab}q), \\ F_{\rm Total} &= \left[\left(F_{\rm Spherical}+F_{\rm Coma}\right)^2+F_{\rm Fabrication}^2\right]^{1/2}, \end{aligned} \tag{2}$$

where $F_{\rm Total}$ is the FWHM focal spot size, Σ is the RMS radiative source size, L is the length of the X-ray footprint, θ_i is the incident angle, p is the distance from the source to the mirror, M is the demagnification (*i.e.* $M = q/p$, where q is the distance from the mirror to the image) and $\Delta_{\rm Fab}$ is the RMS fabrication slope error. The term referred to by Susini *et al.* as the first-order coma represents the minimum focal spot size achievable with an ideal elliptically bent mirror, and corresponds to a demagnified image of the source. Spherical aberration is caused by the mirror's deviation from an ideal elliptical figure and is a strong function of the illuminated mirror length. The contribution due to fabrication error depends linearly on q, the distance from the mirror to the focal plane. Spherical aberration in our application arises from the use of two-point U-benders for both the vertical and horizontal mirrors. When applied to a flat mirror blank, a U-bender produces a cylindrical surface, not an ideal elliptical surface. In equation (2) the contribution due to $F_{\rm Spherical}$ can be regarded as an upper limit since it is calculated using the extreme rays propagated from the mirror surface.

Table 2
Mirror system focus with HHL slits at 1 mm × 1 mm.

The numbers in parentheses indicate values calculated with optically measured mirror slope errors. A slope error of 0.2 μrad RMS for each mirror yields results for the focal spot size that match those measured with the X-ray beam.

Term	Vertical (μm)	Horizontal (μm)
$F_{\rm Coma}$	4.0	85.4
$F_{\rm Spherical}$	14.9	24.5
$F_{\rm Fabrication}$	8.5 (38.1)	5.9 (30.6)
$F_{\rm Total}$	20.7 (42.5)	110.1 (114.1)

The locations of the vertical and horizontal mirrors are 47 m and 49.75 m from the source, respectively, and the nominal focus is located at 56 m, yielding a demagnification of 5.2:1 vertical (M = 0.19) and 8:1 horizontal (M = 0.13). The nominal horizontal and vertical RMS radiative source sizes for sector 14 are $\Sigma_{\rm H}$ = 289.2 μm and $\Sigma_{\rm V}$ = 8.8 μm, respectively (to convert to FWHM, multiply RMS by 2.355). Table 2 lists results calculated for each mirror using equation (2). In this case the HHL slit size was set to 1 × 1 mm and a 3.8 mrad mirror angle was used, producing a footprint of 442 mm on the vertical mirror and 468 mm on the horizontal mirror. A calculation using the metrology results for the slope errors of 0.9 μrad vertical and 1.04 μrad horizontal is shown in parentheses. The experimentally measured spot dimensions, 20 μm vertical by 90 μm horizontal, are smaller than predicted using the specified slope errors. Evidently, the slope error is overestimated for the vertical mirror. Indeed, an assumed slope error of 0.2 μrad in equation (2) more closely matches the measured value of the 20 μm vertical focus size. This discrepancy between the optically measured slope error and that calculated from the observed focal spot size may arise from systematic error in the optical measurement since the X-ray measurements are a direct measure of mirror quality.

Spherical aberration effects on the focal spot size were a concern during design of the beamline owing to the high demagnification ($M < 1$) required to achieve the desired focal spot size. Moreover, unlike a four-point bender, a two-point U-bender does not allow the surface figure to be modified to make it more elliptical. Table 2 shows the relative contributions of each of the effects included in equation (2). When the vertical mirror was ordered, we believed that the dominant contribution to the focal spot width would arise from the specified 1 μrad RMS slope error rather than from spherical aberration. However, the high quality of the mirror surface as fabricated caused the aberration term to become more prominent. While the figure errors are significant compared

with an ideal focus, the reliability and ease of use of the U-bender design still outweigh these concerns.

2.5. X-ray pulse isolation

The time resolution of a pump–probe measurement is determined by the convolution of the pump and probe pulses and the timing jitter between them. Thus, the time resolution depends critically on the ability to cleanly isolate an X-ray probe pulse generated by a single electron bunch and deliver it to the sample at a precise time after the laser pump pulse. The isolation of single X-ray pulses is accomplished at BioCARS by using two beam choppers and a shutter. The choppers rotate continuously and modulate (or chop) the beam in time while the shutter is triggered to open on demand and transmit a single X-ray burst to the sample. A single burst may contain only one ~100 ps X-ray pulse or multiple consecutive pulses depending on the experimental requirements. Each chopper is precisely synchronized with the storage-ring master RF clock at 351.93 MHz using a timing system based on a field programmable gate array (FPGA, see §3.3). The following sections describe the function of each chopper/shutter in greater detail.

2.5.1. HHL chopper. Thermal management is a primary concern in the design of a pink-beam beamline with two in-line undulators. For example, in 24-bunch mode with both undulators tuned to 12 keV the energy in a single focused X-ray pulse is ~20 µJ. With an experimentally measured focal spot size of 90 (H) × 20 (V) µm and a repetition rate of 6.7 MHz (the pulse repetition frequency in 24-bunch mode), the resulting average power density at the sample position is ~74 kW mm^{-2}. For comparison, the surface emission of the sun is 63 W mm^{-2} (Williams, 2004). Static samples cannot tolerate this average flux. Instead of attenuating the pseudo-continuous beam to a level that can be tolerated by samples, we reduce the average power by controlling the duty cycle of the beam with a series of choppers, the most important of which is the HHL chopper. The minimum duty cycle of the HHL chopper is 0.2% resulting in a 500-fold reduction in power. This strategy requires that downstream components tolerate exposure to a single X-ray pulse or to a limited number of pulses in a pulse train.

Though the Jülich chopper (see §2.5.3) rotor can tolerate exposure to the pink beam for a limited period of time, the 135 W average heat load (see Table 1) will eventually overheat the rotor and cause the chopper to shut down. To permit continuous chopper operation, X-ray heating is reduced by a heat-load chopper located upstream of the high-speed chopper (see Fig. 5). The design of this device is based on an air-bearing monochromatic X-ray chopper developed earlier by Professional Instruments Company (PIC) (Minneapolis, MN, USA) in collaboration with the Coppens group (Gembicky *et al.*, 2005). However, to function as a HHL chopper it must be water-cooled, which complicates its design. Fig. 7(*a*) shows a cross section of the chopper rotor: water is supplied through a rotary fluid union and flows down the axis of the spindle in the direction indicated by the red arrow. Use of frictionless air-bearing rotary unions for both the rotor/disc assembly and the fluid connections ensures no mechanical wear at the high operating speed (82.3 Hz), an essential feature for a component expected to log ~5000 h year^{-1}.

Composed of 416 stainless steel, the slotted disc has a diameter of 275 mm and thickness of 7.6 mm, which attenuates the beam by a factor of ~7 × 10^{-21} at 12 keV (Fig. 7*b*). The rotor is located downstream of the HHL slits at 29.2 m, where the maximum power intercepted by the chopper when both undulators are tuned to 12 keV is 520 W. The worst-case temperature rise can be calculated *via* integration of the Laplace equation which assumes a ring-shaped heat source distributed around the circumference of the rotor. This assumption is adequate as long as the characteristic cool-down time τ is greater than the rotational period. The cool-down time can be approximated by

$$\tau = C\rho d^2/\kappa, \qquad (3)$$

where C is the heat capacity, ρ is the density, d is the width of the ring, and κ is the heat conductivity. The characteristic cool-down time given d = 1.5 mm is 0.32 s, which is indeed much greater than the 0.012 s rotational period. For the conditions described above, the rise relative to ambient temperature is 16.5 K, a moderate increase which confirms that the temperature remains well below the melting point of stainless steel.

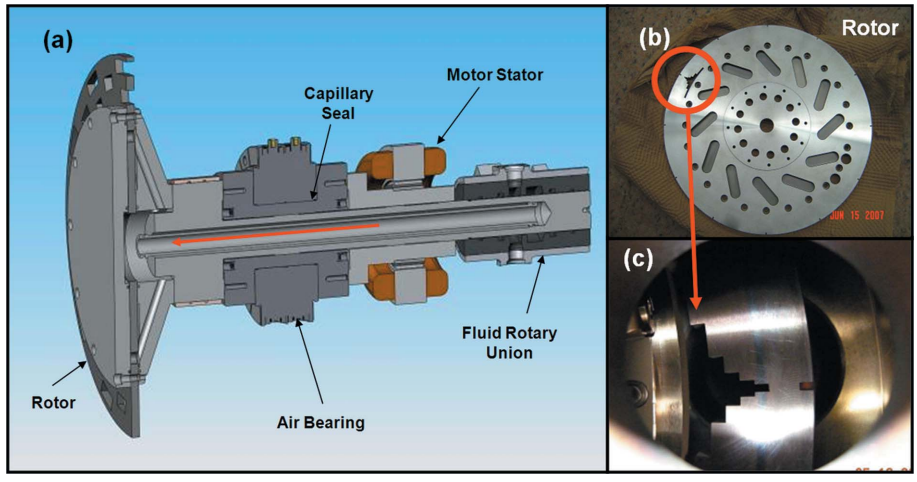

Figure 7
The water-cooled HHL chopper. Panel (*a*) shows a cross-sectional view, in which the X-ray beam impinges on the chopper perpendicular to the rotor surface. An air bearing provides frictionless rotational motion while water flows down the shaft along the center of rotation (red arrow). Panels (*b*) and (*c*) show the rotor and a close-up view of the slot configuration. The entire chopper can be translated horizontally to choose different slot widths. The location of the beam port behind the slotted disc in panel (*c*) is at the 3 o'clock position of panel (*a*).

Fig. 7(*c*) shows a magnified view of the slotted disc. At a fixed rotation frequency of 82.3 Hz the twelve 1.5 mm slots located around the circumference of the rotor produce a pulse train at a frequency of 987.4 Hz with an open time of 22 µs for each burst. On the interior of the rotor there is one set of six stepped slots with widths of 1.5, 3, 6, 12, 24 and 48 mm. The repetition frequency for these slots is 82.3 Hz and produce opening times that range from 22 µs to 789 µs, thereby producing open duty cycles between 0.2% and 6.5%. For most experiments the 0.2% duty cycle is used, which reduces the downstream X-ray power to 1.04 W, and reduces the heat load on the Jülich chopper to 270 mW. This major reduction in heat load on the downstream optics eliminates thermal drift of the mirror alignment and allows continuous operation of the Jülich chopper. The opening of the HHL and the Jülich choppers are synchronized to within 17 ns, the jitter of the HHL chopper.

2.5.2. Millisecond shutter. As noted above, the HHL chopper produces bursts of storage-ring pulses with a repetition rate of 82.3 Hz. The millisecond shutter, which is located in the 14-ID-B station, is capable of isolating, on demand, single X-ray bursts from the HHL chopper at frequencies up to 41.2 Hz. The ∼12 ms period between bursts sets an upper limit on the opening time for the millisecond shutter. The millisecond shutter employs a low-inertia slotted block that is driven by a servo motor, and can be triggered to isolate single pulses or a burst of pulses from the HLL and Jülich choppers at a rate up to half the ∼82.3 Hz chopping frequency of the HLL chopper. The slotted block is shown schematically in Fig. 2. The opening time of the millisecond shutter is a function of repetition frequency; opening times <1 ms are possible when operated at lower repetition frequencies (details to be published elsewhere).

2.5.3. Jülich chopper. At the heart of the X-ray pulse isolation system is the Jülich chopper, which was designed and manufactured by Forschungszentrum Jülich (Germany). The rotor and electronics of the original Jülich chopper in use at BioCARS since 2000 have been upgraded to our specifications to facilitate isolation of a single X-ray pulse from the APS in both 24-bunch and hybrid modes. A magnetic bearing levitates the shaft of a titanium triangular rotor and allows it to spin friction-free at a nominal rate of 987 Hz. A photograph of the chopper with the rotor exposed is shown in Fig. 8(*a*). The beam is transmitted in only one orientation of the rotor, either through a tunnel or in tunnel-less mode. The relationships describing the chopper opening as a function of time in tunnel-less mode are presented by Cammarata *et al.* (2009), as in equations (4) and (5),

$$\Delta t_{\rm top} = \frac{2h - s}{3^{1/2}\pi f R}, \tag{4}$$

$$\Delta t_{\rm base} = \frac{2h + s}{3^{1/2}\pi f R}, \tag{5}$$

where the radius of the rotor R is measured from the center to the outermost tip; h is the distance of the X-ray beam above the surface of the rotor; s is the vertical height of the X-ray beam; and f is the rotation frequency. Fig. 8(*b*) shows a schematic drawing of the rotor and the parameters that appear in the open-time equations while Fig. 8(*c*) shows a plot of opening *versus* time.

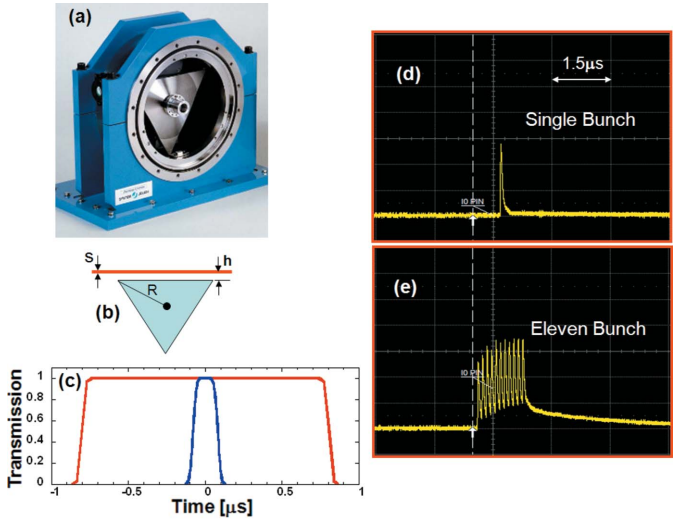

Figure 8
The Jülich chopper. Panel (*a*) shows a photograph of the chopper with its vacuum flange removed. Panel (*b*) shows a schematic of its triangular rotor. The open time function, shown in panel (*c*), has a trapezoidal shape and, by changing h, the distance to the center of the X-ray beam from the rotor edge, the opening time can be set to transmit only one [panel (*d*)] or several [panel (*e*)] X-ray pulses.

The perennial limitation on short-pulse pink-beam X-ray experiments at BioCARS was the brief availability of the hybrid operating mode at the APS, a mode typically limited to two weeks per three-month run. Hybrid mode was specifically created with 1.59 µs 'gaps' on either side of the 16 mA bunch (see Fig. 3), which simplified isolation of a single X-ray pulse with a mechanical chopper. In contrast, the pulse separation in 24-bunch mode, the common operating mode at the APS, is only 153.4 ns. In the past, the opening time and jitter of the original Jülich chopper limited ultrafast time-resolved experiments to the hybrid mode. However, two improvements to the beamline have made single-pulse isolation possible in 24-bunch mode. The new KB mirror system (discussed in §2.3.2) produces a vertical focus as small as 20 µm, significantly improved over that achieved previously. Moreover, improvements in the chopper control electronics reduce the timing jitter to 2.3 ns RMS. The benefits of these improvements are made clear in equations (4) and (5). For the Jülich chopper, R = 96.8 mm and f = 987 Hz. Typically, for single-bunch isolation, h = 35 µm and s = 40 µm (the vertical focus is usually positioned at the mid-point between the chopper and the JJ-slits (see Fig. 9), which enlarges s at the chopper position to 40 µm). With these parameters, $t_{\rm base}$ = 212 ns and $t_{\rm top}$ = 58 ns, giving a base half-width of 106 ns, which is well within the 153.4 ns inter-bunch spacing. Owing to the improved focal-spot size and chopper control electronics, it is straightforward to isolate a single X-ray pulse from the 24-bunch mode.

A unique feature of the triangular rotor in tunnel-less mode is the ability to change the opening time of the chopper by

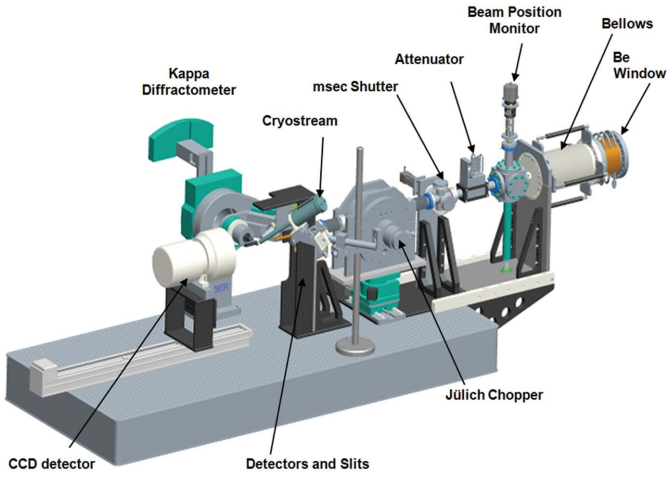

Figure 9
The table and experimental apparatus in the 14-ID-B hutch. These are shown as a three-dimensional solid model for clarity. The center of the kappa diffractometer is located 56 m from the source point (see Fig. 5).

simply raising or lowering the top surface of the rotor relative to the X-ray beam, thus changing h. Figs. 8(d) and 8(e) show two oscilloscope traces recorded by the I_0 pin diode (see §3) for single-pulse isolation and 11-pulse isolation. In 11-pulse mode a value of h = 400 µm gives t_{base} = 1.62 µs and t_{top} = 1.46 µs.

3. Experimental set-up

The experimental set-up located at station 14-ID-B is represented in Fig. 9 by a three-dimensional solid model. Starting from the right, a large-aperture 0.5 mm-thick beryllium window (Brush Wellman Electrofusion Products) separates the KB mirror vacuum segment from the experimental apparatus. To reduce mechanical stress when supporting an external pressure up to 1 atm, the beryllium window was brazed to a convex cylindrical frame with a 101.6 mm radius of curvature. With a clear aperture of 44 mm (H) × 90 mm (V), this window accommodates the direct white beam and all possible mirror angles up to 4 mrad in each direction.

The components in Fig. 9 are mounted on an optical table that is motorized with six degrees of freedom (three translational, x, y and z, plus pitch, roll and yaw angles). A change in both KB-mirror angles is coupled to combined motions of the table to follow the X-ray beam trajectory. Additionally, since the distance from the X-ray beam to the top of the Jülich chopper rotor must be maintained to within a few micrometers in order to isolate single pulses cleanly (see §2.5.3), the optical table must be stable to the same degree. The position of the monochromatic beam is measured by a fluorescence-based beam-position monitor (BPM) (Alkire *et al.*, 2000). An attenuator box is located downstream of the BPM, followed by the millisecond shutter and Jülich chopper. Two Huber mechanical stages provide horizontal and vertical motion of the Jülich chopper. The vertical motion changes the chopper open time in tunnel-less mode, and the horizontal motion selects the chopper mode: bypass, tunnel-less or tunnel chopping modes. A rigid pedestal downstream of the Jülich chopper supports an in-vacuum four-blade JJ-slit (manufactured by JJ X-ray, Denmark) assembly and non-invasive diagnostic X-ray detectors. The layout is shown schematically in Fig. 10, in which the X-ray beam traverses the components from right to left. A 10 mm-diameter beryllium window separates the vacuum segment required by the Jülich chopper from atmospheric pressure on the detector side. Two X-ray-sensitive detectors are located downstream of the beryllium window. A Bicron BC422Q scintillator coupled to a microchannel plate photomultiplier is positioned just below the X-ray beam; it detects scattered radiation from the Be window and produces pulses with a 275 ps rise time. This detector is used to record non-invasively the pump–probe delay for each measurement during an experiment. The second detector, a PIN diode manufactured by Canberra (model ANFD300-20-300RM) with a 4 mm beam-pass-through hole at its center, is relatively slow but provides pulse intensity information on a pulse-by-pulse basis for I_0 normalization.

For conventional synchrotron beamlines, where the X-ray flux is considered to be quasi-continuous, an integrating detector such as an ion chamber is often used to measure the beam intensity. The readout electronics for these detectors typically consists of a transimpedance amplifier followed by a voltage-to-frequency converter and a computer-controlled counter. Such an approach does not work well for this time-resolved beamline, where the average current produced by the chopped X-ray beam is very low but the peak current is sufficiently high to easily saturate a transimpedance amplifier. Instead, we use a digital oscilloscope (LeCroy WaveSurfer) to digitize and integrate the area under the signal generated by each X-ray pulse from the I_0 detector. The area is proportional to the total charge collected and therefore to the number of

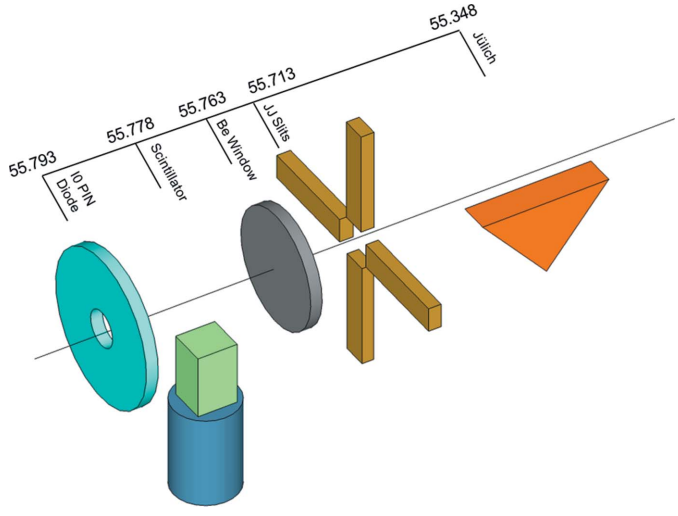

Figure 10
Schematic view of the high-speed chopper, clean-up slits and non-invasive X-ray detectors, which record simultaneous shot-by-shot X-ray flux and pulse time-of-arrival signals during data collection. The scale shows the position in meters of each component measured from the source point (see Fig. 5).

photons in the X-ray pulse. An EPICS (Experimental Physics and Industrial Control System) application running directly on the oscilloscope makes it resemble a standard EPICS detector, whose output can be recorded in conjunction with any other EPICS device, for example, one of the instrument positioners.

The goniometer is a standard Huber 515.2 kappa model in which a motorized *XYZ*-translation stage mounted on the φ-stage facilitates centering of the crystal. Two microscope CCD cameras with 1 μm and 6 μm resolution are mounted to the rigid pedestal and are used to aid in crystal centering. Diffracted X-rays are imaged on a CCD detector (at present a MAR165 CCD) mounted on a 0.8 m-long Velmex dovetail translation stage used to adjust the crystal-to-detector distance. The MAR165 CCD is a 165 mm-diameter phosphor-coupled CCD detector and is run in 2×2 pixel binning mode with an effective pixel size of 80 μm. The MAR165 CCD has a full well capacity of 45000 photons pixel^{-1} at 12 keV and a readout time of 2.5 s per frame. For typical crystals of small molecules or for a well ordered crystal of small biological macromolecules, it is possible to saturate a single pixel with diffracted beam produced by one 100 ps X-ray pulse in 24-bunch mode. This corresponds to an instantaneous flux $>4.5 \times 10^{14}$ photons s^{-1} pixel^{-1} at the most intense region of the Bragg spot. This flux is far beyond the capabilities of any photon-counting pixel-array detector presently available commercially. Thus, an integrating detector with a large well capacity is best suited for these time-resolved experiments.

3.1. Laser systems

Two laser systems are presently operational and available for BioCARS users: a modified Spectra-Physics (SP) Spitfire Pro picosecond laser coupled to a TOPAS optical parametric amplifier (OPA), and a nanosecond OPOTEK Nd:YAG/optical parametric oscillator (OPO). The SP picosecond laser enables picosecond time resolution for the first time at BioCARS. Both lasers are housed in an external temperature-stabilized laser hutch. Picosecond laser pulses are transported to the 14-ID-B X-ray station by mirrors while nanosecond laser pulses are transported *via* fiber optics.

The SP picosecond laser system is composed of several components. A SP Millennia CW laser pumps a SP Tsunami mode-locked Ti:sapphire laser which generates a femtosecond seed beam for the Spitfire Pro. This seed beam is spectrally narrowed to about 12.5 cm^{-1} FWHM bandwidth to produce transform-limited ∼1.2 ps seed pulses. The Spitfire Pro enclosure contains both a Ti:sapphire regenerative preamplifier and a double-pass Ti:sapphire power amplifier, each of which is pumped by a SP Empower laser. The seed pulses are stretched, amplified, then compressed to produce ∼1.2 ps pulses at 780 nm with an energy of 5 mJ and a repetition frequency up to 1 kHz. The amplified pulses pump the TOPAS OPA, which produces tunable signal and idler pulses. Nonlinear mixing schemes such as second-harmonic generation of the signal or idler pulses or sum-frequency mixing of the signal or idler pulses with the residual pump beam extends the tunability from greater than 2000 nm down to ∼450 nm with >300 μJ pulse energy. The multi-wavelength TOPAS output is passed through a set of dichroic mirrors to isolate the desired wavelength, which is transported ∼30 m to the 14-ID-B station by a periscope mirror system.

Table 3
BioCARS laser parameters.

Laser	Wavelength	Pulse width	Maximum repetition rate	Energy/power
Millennia	532 nm	CW	CW	5 W
Tsunami	780 nm	100 fs	70 MHz	850 mW
Empower	527 nm	300 ns	1 kHz	15 mJ
Spitfire Pro	780 nm	1.2 ps	1 kHz	5 mJ
TOPAS	450–2000 nm	1.2 ps	1 kHz	>150 μJ (at sample)
OPOTEK	250–2000 nm	6 ns	10 Hz	∼150 μJ (at sample with 300 μm fiber delivery)

Laser beam-conditioning optics located above the diffractometer in station 14-ID-B stretch the pulses to 35 ps in an echelon and, depending on the experimental requirements, are focused to either a circular or elliptical focal spot. The polarization of the laser pulse (linear or circular) is controlled *via* a New Focus Berek compensator located before the final focusing optic. Two computer-controlled gradient neutral density filters adjust the laser power at the sample.

A broadly tunable Vibrant laser system (OPOTEK), which generates ∼4 ns laser pulses (FWHM), is also available. The frequency-tripled output from a flash-lamp-pumped Nd:YAG laser pumps an OPO to produce pulses tunable from 400 to 650 nm at 10 Hz with ∼35 mJ pulse^{-1}. With appropriate modules this output can be frequency doubled to produce UV pulses from 240 to 380 nm with an average energy of 4 mJ pulse^{-1}. The beam is presently transported to the laser hutch *via* a 30 m-long optical fiber of diameter 300 μm which limits the pulse energy at the sample to ∼150 μJ. The laser beam is focused further to 200 μm diameter, providing power densities at the sample of up to ∼4.8 mJ mm^{-2}. Table 3 lists the pulse parameters for the lasers.

3.2. Experimental geometry and timing

To maximize the extent of photoactivation in pump–probe time-resolved X-ray measurements, it is crucial to match the penetration depth of the laser to that of the X-ray beam. To that end, we employ an orthogonal pump–probe geometry and tune the laser wavelength so that its optical penetration depth is comparable with the vertical spot size of the X-ray beam. A 25 μm tungsten pinhole mounted on the goniometer is used to align the laser and X-ray beams. The pinhole is first positioned at the goniometer center of rotation with the horizontal φ rotation axis perpendicular to both X-ray ($+z$) and laser beam ($-y$) directions. Next, the cross hairs for microscope cameras oriented at two different angles (+30° and +60°) relative to the X-ray beam are centered on the pinhole. To align the X-ray beam, the pinhole is rotated to transmit the X-ray beam and the KB mirror angles are adjusted to maximize transmission through the pinhole. The dimensions of the X-ray beam can be

recorded by mounting a small phosphor screen on the goniometer center of rotation and measuring the X-ray spot profile observed on the microscope camera. The laser beam steering motors position the laser focal spot at the center of the microscope cross hairs. Centering the sample on the microscope cross hairs is sufficient to ensure optimal spatial overlap between the pump and probe pulses. The laser position suffers from long-term drift owing to the >30 m path separating the laser and X-ray hutches. To compensate for this drift, the sample is periodically retracted from the beam and an additional microscope camera mounted underneath the crystal records the laser beam position; position errors exceeding about 10% of the beam size are corrected.

Once spatial overlap is achieved, the relative time of arrival Δt of the laser pump and X-ray probe pulses is measured and used to calibrate the time delay. This measurement employs a fast Hamamatsu metal–semiconductor–metal InGaAs photodetector (G7096 series) positioned at the goniometer center of rotation and read out using an Agilent Infiniium 6 GHz 40 GSa s^{-1} oscilloscope (details to be published elsewhere). The precision of the time delay is limited by the 10 ps resolution of a digital delay generator. The RMS jitter of the measurement was found to be <10 ps, a value small compared with the ~100 ps duration X-ray pulse.

3.3. FPGA control and synchronization

As discussed in previous sections, synchrotron-based pump–probe time-resolved techniques require precise synchronization of multiple X-ray shutters and laser triggers. Additionally, it is also important to be able to quickly change the time delay between the X-ray and laser pulses. These goals have been achieved through the use of a Xilinx Virtex-II Pro field-programmable gate array (FPGA) with an imbedded PowerPC processor. The FPGA technology was implemented *via* a Suzaku-V FPGA project kit from Atmark Techno that integrates the Xilinx chip into a complete package running Linux with an Ethernet interface and external memory. In addition, an external GigaBaudics, 3 GHz Programmable Delay Line, model PADL3-10-11, is used to generate pump–probe delays over a 20.47 ns range with 10 ps resolution.

All timing is synchronized to the 271.55 kHz P0 signal and 43.99 MHz (storage-ring RF frequency divided by 8) signal provided to every beamline by the APS. The P0 signal provides one pulse every storage-ring orbital period, and is used to phase the FPGA output signals. The 44 MHz signal is multiplied by 8 to produce the original 351.93 MHz RF frequency, which is then divided down to generate all of the sub-harmonic frequencies required to synchronize the chopper controllers, laser mode locker and various triggers.

3.4. Control software and user interfaces

Beamline hardware such as stepper motors, counters, analog-to-digital converters, *etc.* are controlled using the EPICS package developed in part at the APS. For high-level data acquisition two software packages, written in-house, are routinely used at BioCARS. *LaueCollect* has been developed primarily for time-resolved pink-beam experiments while *xControl* is employed mostly for monochromatic data collection. Both programs are written in Python and utilize channel access to communicate with EPICS *via* the *CaPython* wrapper (KEK Accelerator Laboratory, Japan). Each program serves as an interface to the MAR165 CCD detector to collect and read out CCD frames and rotate the sample on the goniometer.

4. Conclusions

The upgraded beamline has performed very well and is operating close to theoretical predictions with the X-ray flux density at the sample being increased almost 100-fold. With the original beamline configuration, macromolecular crystals such as photoactive yellow protein (PYP) required over 80 pump–probe cycles per CCD frame to achieve sufficient intensity in the weaker Bragg peaks. A typical PYP crystal now has roughly one-tenth of its volume illuminated owing to the reduced X-ray focal spot size when compared with the previous set-up. Only eight pump–probe cycles per CCD frame are required for a typical PYP crystal, decreasing the number of cycles by a factor of ten. Since the number of molecules in the crystal contributing to diffracted intensity has been reduced by ten owing to the volume reduction and the X-ray flux density has increased by a factor of 100, the overall increase in Bragg intensity per shot is ten. For PYP, this results in significantly reduced data collection times since these crystals require several seconds waiting time between laser-pump pulses to allow for molecular relaxation to the initial dark state at room temperature (Schmidt *et al.*, 2010). Additionally, the relatively small beam sizes allow a single crystal to be probed at multiple sites along its length by translating it relative to the X-ray/laser beam intersection, thus reducing the number of crystals needed for obtaining comprehensive time-resolved data, spanning a sufficient number of time points.

Several publications describe recent studies that utilize the enhanced capabilities at BioCARS. Five-dimensional crystallography by Schmidt *et al.* (2010) describes an experimental approach for determining a comprehensive chemical mechanism in macromolecular reactions. It utilizes temperature-dependent time-resolved X-ray diffraction measurements. Feasibility studies examined the PYP photocycle. Wide-angle X-ray scattering (WAXS) of macromolecules in solution is becoming a standard tool for the biological X-ray scattering community. Cho *et al.* (2010) present a time-resolved pump–probe variant of this technique applied to dilute solutions of myoglobin. In these experiments the carbon monoxy form of myoglobin (MbCO) is photolyzed by a short laser pulse and the structural changes are tracked with 100 ps time resolution as the molecule transitions from MbCO form to deoxy (Mb) form.

Small-molecule chemical crystallography studies aimed at extracting excited-state structures (Coppens *et al.*, 2010; Kamiński *et al.*, 2010) have been carried out on $Cu_4I_4(pip)_4$ (pip = piperidine, $C_5H_{10}NH$). Small-molecule crystals typically diffract better than macromolecular crystals and require only

Table 4
Summary of beamline parameters.

Beamline name	BioCARS 14-ID
Source type	Two collinear undulators with 23 and 27 mm periods
Mirrors	KB pair with 1 m longitudinal length
Monochromator	Cryogenically cooled Si (111)
Monochromatic energy range	6.8–19 keV (1.82–0.65 Å)
Goniometer	Kappa
Cryo capability	Liquid-nitrogen cryostream
Detector type	MAR165 CCD, a 165 mm-diameter phosphor-coupled CCD
X-ray parameters	
First-harmonic energy range	6.8–19 keV
Photons per pulse (24 bunch mode at 12 keV)	1.1×10^{10} photons (pink beam)
Photons per pulse (hybrid mode at 12 keV)	4.2×10^{10} photons (pink beam)
Minimum focal spot size	90 μm (H) × 20 μm (V)
Pulse width (FWHM)	79 and 118 ps
Laser parameters	
Wavelength range	2000–250 nm
Nominal pulse energy at sample	>150 μJ
Focal spot size at sample	∼100 μm diameter and 100 μm × 600 μm elliptical
Pulse flux at sample	>3 mJ mm^{-2}
Pulse width (FWHM)	1.2 ps, 35 ps and 6 ns

a single pump–probe cycle per CCD frame. For these atomic-resolution measurements of chemical processes the accuracy and repeatability to which a diffraction spot intensity is measured is critical. Kamiński *et al.* (2010) show that the beamline stability is quite good and Bragg intensities reproduce to within 2–3%.

In addition to crystallography and WAXS the beamline has been used to study time dependence of non-equilibrium phonons in InP and InSb after laser irradiation using an X-ray diffuse-scattering technique to image lattice vibrations (Trigo *et al.*, 2010). In these studies both InP and InSb exhibit strong and complex non-equilibrium redistributions of scattered intensity that persists several hundred picoseconds after excitation. Using singular value decomposition, a delayed increase in the transverse-acoustic (TA) phonon population in InP is clearly shown along with a decrease in the longitudinal-acoustic phonons. This population increase is most significant along the high-symmetry ⟨111⟩ and ⟨010⟩ directions. However, in InSb the TA phonon population is less directional and is distributed more isotropically within the Brillouin zone.

A novel approach to Mössbauer spectroscopy with synchrotron radiation has been carried out at BioCARS (Toellner *et al.*, 2011). Mössbauer spectroscopy until now has been performed with high-energy-resolution X-ray monochromators that reduce the bandwidth of the exciting X-ray beam thereby allowing the discrimination of the weak decay radiation from the prompt exciting beam. These monochromators are limited to a relatively small range of energies and therefore limit the number of Mössbauer active elements to those within this range. A new method for performing this experiment in which the Jülich chopper is used to block the prompt radiation has been demonstrated using the 14-ID pulse-isolating system. This new technique will allow the use of standard monochromators for these measurements thus opening the possibility to study compounds with a wide range of Mössbauer active elements.

Each of the four goals for the beamline upgrade described in the *Introduction* has been met. We are able to produce high-quality Laue diffraction data and have extended single bunch operation with ∼100 ps time resolution to almost 80% of the available APS beam time. Table 4 summarizes the beamline parameters most relevant for the preparation of an experiment at BioCARS. The X-ray optics are performing close to theoretical predictions and produce a focal spot size of 90 μm horizontal by 20 μm vertical. This small vertical beam size has enabled single X-ray pulse isolation with up to 4×10^{10} photons pulse^{-1} at 12 keV.

Use of the Advanced Photon Source was supported by the US Department of Energy, Basic Energy Sciences, Office of Science, under Contract No. DE-AC02-06CH11357. Use of the BioCARS sector 14 was supported by the National Institutes of Health, National Center for Research Resources, under grant number RR007707. The time-resolved set-up at sector 14 was funded in part by NIH/NIDDK. We thank all APS personnel who supported this upgrade project, specifically Efim Gluskin, Roger Dejus and Elizabeth Moog for collaborating on the design of the new undulator system and partially funding its procurement. We also thank Dana Capatina and Yifei Jaski for their FEA analysis of the HHL components, and Troy Lutes, our APS interface for the project. We also wish to acknowledge former BioCARS staff Michael Bolbat and Jay VonOsinski for their expert assistance during the 14-ID upgrade.

References

Alkire, R. W., Rosenbaum, G. & Evans, G. (2000). *J. Synchrotron Rad.* **7**, 61–68.
Anderson, S., Šrajer, V., Pahl, R., Rajagopal, S., Schotte, F., Anfinrud, P., Wulff, M. & Moffat, K. (2004). *Structure*, **12**, 1039–1045.
Bourgeois, D., Ursby, T., Wulff, M., Pradervand, C., Legrand, A., Schildkamp, W., Labouré, S., Srajer, V., Teng, T. Y., Roth, M. & Moffat, K. (1996). *J. Synchrotron Rad.* **3**, 65–74.
Bourgeois, D., Vallone, B., Arcovito, A., Sciara, G., Schotte, F., Anfinrud, P. A. & Brunori, M. (2006). *Proc. Natl Acad. Sci. USA*, **103**, 4924–4929.
Bourgeois, D., Vallone, B., Schotte, F., Arcovito, A., Miele, A. E., Sciara, G., Wulff, M., Anfinrud, P. & Brunori, M. (2003). *Proc. Natl Acad. Sci. USA*, **100**, 8704–8709.
Cammarata, M., Eybert, L., Ewald, F., Reichenbach, W., Wulff, M., Anfinrud, P., Schotte, F., Plech, A., Kong, Q., Lorenc, M., Lindenau, B., Räbiger, J. & Polachowski, S. (2009). *Rev. Sci. Instrum.* **80**, 015101.
Cho, H. S., Dashdorj, N., Schotte, F., Graber, T., Henning, R. & Anfinrud, P. (2010). *Proc. Natl Acad. Sci. USA*, **107**, 7281–7286.
Coppens, P., Benedict, J., Messerschmidt, M., Novozhilova, I., Graber, T., Chen, Y.-S., Vorontsov, I., Scheins, S. & Zheng, S.-L. (2010). *Acta Cryst.* A**66**, 179–188.
Gembicky, M., Oss, D., Fuchs, R. & Coppens, P. (2005). *J. Synchrotron Rad.* **12**, 665–669.
Genick, U. K., Borgstahl, G. E., Ng, K., Ren, Z., Pradervand, C., Burke, P. M., Srajer, V., Teng, T. Y., Schildkamp, W., McRee, D. E., Moffat, K. & Getzoff, E. D. (1997). *Science*, **275**, 1471–1475.

Ihee, H., Rajagopal, S., Šrajer, V., Pahl, R., Anderson, S., Schmidt, M., Schotte, F., Anfinrud, P. A., Wulff, M. & Moffat, K. (2005). *Proc. Natl Acad. Sci. USA*, **102**, 7145–7150.
Kamiński, R., Graber, T., Benedict, J. B., Henning, R., Chen, Y.-S., Scheins, S., Messerschmidt, M. & Coppens, P. (2010). *J. Synchrotron Rad.* **17**, 479–485.
Knapp, J. E., Pahl, R., Šrajer, V. & Royer, W. E. (2006). *Proc. Natl Acad. Sci. USA*, **103**, 7649–7654.
Krasnicki, K. (1996). *Rev. Sci. Instrum.* **67**, 3369.
Mochizuki, T., Kohmura, Y., Awaji, A., Suzuki, Y., Baron, A., Tamasaku, K., Yabashi, M., Yamazaki, H. & Ishikawa, T. (2001). *Nucl. Instrum. Methods Phys. Res. A*, **467–468**, 647–649.
Moffat, K. (1989). *Annu. Rev. Biophys. Biophys. Chem.* **18**, 309–332.
Moffat, K., Szebenyi, D. & Bilderback, D. (1984). *Science*, **223**, 1423–1425.
Nozawa, S., Adachi, S., Takahashi, J., Tazaki, R., Guérin, L., Daimon, M., Tomita, A., Sato, T., Chollet, M., Collet, E., Cailleau, H., Yamamoto, S., Tsuchiya, K., Shioya, T., Sasaki, H., Mori, T., Ichiyanagi, K., Sawa, H., Kawata, H. & Koshihara, S. (2007). *J. Synchrotron Rad.* **14**, 313–319.
Perman, B., Srajer, V., Ren, Z., Teng, T., Pradervand, C., Ursby, T., Bourgeois, D., Schotte, F., Wulff, M., Kort, R., Hellingwerf, K. & Moffat, K. (1998). *Science*, **279**, 1946–1950.
Rajagopal, S., Schmidt, M., Anderson, S., Ihee, H. & Moffat, K. (2004). *Acta Cryst.* D**60**, 860–871.
Ren, Z., Bourgeois, D., Helliwell, J. R., Moffat, K., Šrajer, V. & Stoddard, B. L. (1999). *J. Synchrotron Rad.* **6**, 891–917.
Ren, Z., Perman, B., Srajer, V., Teng, T. Y., Pradervand, C., Bourgeois, D., Schotte, F., Ursby, T., Kort, R., Wulff, M. & Moffat, K. (2001). *Biochemistry*, **40**, 13788–13801.
Sánchez del Río, M. & Dejus, R. J. (2004). *AIP Conf. Proc.* **705**, 784–787.
Schmidt, M., Graber, T., Henning, R. & Srajer, V. (2010). *Acta Cryst.* A**66**, 198–206.
Schmidt, M., Nienhaus, K., Pahl, R., Krasselt, A., Anderson, S., Parak, F., Nienhaus, G. U. & Šrajer, V. (2005). *Proc. Natl Acad. Sci.* **102**, 11704–11709.
Schotte, F., Lim, M., Jackson, T. A., Smirnov, A. V., Soman, J., Olson, J. S., Phillips, G. N., Wulff, M. & Anfinrud, P. A. (2003). *Science*, **300**, 1944–1947.
Schotte, F., Soman, J., Olson, J. S., Wulff, M. & Anfinrud, P. A. (2004). *J. Struct. Biol.* **147**, 235–246.
Srajer, V., Ren, Z., Teng, T. Y., Schmidt, M., Ursby, T., Bourgeois, D., Pradervand, C., Schildkamp, W., Wulff, M. & Moffat, K. (2001). *Biochemistry*, **40**, 13802–13815.
Srajer, V., Teng, T., Ursby, T., Pradervand, C., Ren, Z., Adachi, S., Schildkamp, W., Bourgeois, D., Wulff, M. & Moffat, K. (1996). *Science*, **274**, 1726–1729.
Susini, J. (1995). *Opt. Eng.* **34**, 361.
Susini, J. & Wulff, M. (1993). *Proc. SPIE*, **1997**, 278–289.
Toellner, T. S., Alp, E. E., Graber, T., Henning, R. W., Shastri, S. D., Shenoy, G. & Sturhahn, W. (2011). *J. Synchrotron Rad.* **18**, 183–188.
Trigo, M., Chen, J., Vishwanath, V. H., Sheu, Y. M., Graber, T., Henning, R. & Reis, D. A. (2010). *Phys. Rev. B*, **82**, 235205.
Uruga, T., Tanida, H., Yoneda, Y., Takeshita, K., Goto, S. & Ishikawa, T. (2001). *Nucl. Instrum. Methods Phys. Res.* **467–468**, 782–784.
Williams, D. R. (2004). *NASA Sun Fact Sheet Web Page*, http://nssdc.gsfc.nasa.gov/planetary/factsheet/sunfact.html.
Wulff, M., Plech, A., Eybert, L., Randler, R., Schotte, F. & Anfinrud, P. (2002). *Faraday Discuss.* **122**, 13–26.